Short-wavelength interband cascade infrared photodetectors operating above room temperature

Hossein Lotfi,[1] Lu Li,[1] Lin Lei,[1,2] Yuchao Jiang,[1] Rui Q. Yang,[1] John F. Klem,[3] and Matthew B. Johnson[2]

[1]*School of Electrical and Computer Engineering, University of Oklahoma, Norman, Oklahoma 73019, USA*
[2]*Homer L. Dodge Department of Physics and Astronomy, University of Oklahoma, Norman, Oklahoma 73019, USA*
[3]*Sandia National Laboratories, Albuquerque, New Mexico 87185, USA*

High temperature operation (250–340 K) of short-wavelength interband cascade infrared photodetectors (ICIPs) with $InAs/GaSb/Al_{0.2}In_{0.8}Sb/GaSb$ superlattice absorbers has been demonstrated with a 50% cutoff wavelength of 2.9 μm at 300 K. Two ICIP structures, one with two and the other with three stages, were designed and grown to explore this multiple-stage architecture. At $\lambda = 2.1\,\mu$m, the two- and three-stage ICIPs had Johnson-noise-limited detectivities of 5.1×10^9 and $5.8 \times 10^9\,cm\,Hz^{1/2}$/W, respectively, at 300 K. The better device performance of the three-stage ICIP over the two-stage ICIP confirmed the advantage of more stages for this cascade architecture. An Arrhenius activation energy of 450 meV is extracted for the bulk resistance-area product, which indicates the dominance of the diffusion current at these high temperatures. © 2016 AIP Publishing LLC.
[http://dx.doi.org/10.1063/1.4939961]

I. INTRODUCTION

Short-wavelength infrared (SWIR) detectors have many military and civilian applications including low photon flux detection, medical diagnostics, optical communications, low-light night vision, security, produce inspection, and remote sensing. SWIR (1–3 μm) is an important "color" in the terrestrial transmission windows of the IR that also includes mid-wave IR (MWIR at 3–5 μm), long-wave IR (LWIR at 8–12 μm), and very long wave IR (VLWIR at >14 μm). Detecting multiple bands (colors) has advantages for more versatile detection and imaging, and such multi-color detectors have much promise. As far as SWIR technologies, InGaAs is very mature, but cannot be extended to other IR colors. Mercury cadmium telluride (MCT) is mature and works over all IR colors; however, MCT has limitations associated with irregular substrates and their availability, the complexity of materials growth and fabrication. Type-II superlattice (SL) is a band engineered material system based on the more robust III-V materials. Type-II InAs/GaSb SL detectors can cover the SWIR to VLWIR wavelength range with predicted superior performance compared to $Hg_{1-x}Cd_xTe$.[1,2] While extensive research on the mid- to very-long-wave type-II SL IR detectors has shown some promising results, there has been limited research on the SWIR band operating at high temperatures.[3–5] Issues such as relatively short diffusion length, carrier lifetime, and small absorption coefficient are still open problems in type-II SL detectors. While the first two will be improved by better material quality, the latter is intrinsic to type-II SL material system. This small absorption coefficient can be compensated by a thicker absorber; however, photo-response may not increase accordingly; and noise will increase proportionally with the length of the absorber.[6,7] These limitations can be mitigated in a multiple-stage discrete absorber architecture in which individual absorbers are separated by unipolar barriers and the thickness of every absorber is kept shorter than the diffusion length of minority carriers. In the multiple-stage discrete absorber architecture, photo-generated carriers travel across only one cascade stage before they recombine and are collected at the interfaces of adjacent stages or the two end contacts. Hence, the total thickness of absorbers in a multiple-stage detector can be longer than the diffusion length and can also be tuned in such a way to absorb most of the IR photons in the desired spectral band. Interband cascade infrared photodetectors (ICIPs) are constructed based on such a multiple-stage architecture by utilizing unique band alignments in the InAs/GaSb/AlSb material system, with each stage composed of two selective barriers (called electron and hole barriers) on the two sides of an absorber. Additionally, ICIPs have other advantages such as high device resistance, reduced shot noise, feasibility to perform well at high temperatures, and high speed operation without compromising sensitivity.[7,8] ICIPs for the MWIR to VLWIR ranges have been demonstrated,[8–11] but there has been no work on SWIR ICIPs. An SWIR ICIP can be a stand-alone detector or can be integrated with MWIR, LWIR, and/or VLWIR detectors to realize multi-color ICIPs. Thus, ICIPs are viable for a multi-color detector implementation in a wide range of the IR spectrum. For example, ICIPs with regular and reverse configurations (photogenerated carriers travel in opposite directions) that have been reported[10,11] can be integrated to realize a bias selectable two-color ICIP. In this work, we demonstrate SWIR ICIPs working in the 250–340 K temperature range with cutoff wavelength near 3 μm. We investigate two- and three-stage ICIPs to explore the influence of the number of stages on the detector characteristics for 250–340 K.

This paper is organized as follows: in Section II we give details on the design, growth, and fabrication of the two ICIPs. This is followed by Results and Discussion, starting with electrical characteristics and followed with optical

characteristics. Finally, the paper is concluded with some discussion on the observed benefits of the multiple-stage structure and future work on SWIR ICIPs.

II. DEVICE DESIGN, GROWTH, AND FABRICATION

A. Device design and structure

Short cutoff wavelengths ($<3\,\mu m$) can be directly achieved using thin InAs layers in a two-constituent InAs/GaSb SL. However, thin InAs layers add some complexity to the growth process in terms of interface mixing/roughness and make the device bandgap very sensitive to the thickness variations in time and space (uniformity) during growth. Difficulties such as lower material and interface quality have been reported in the literature.[3,4] Furthermore, although thinning each InAs layer in the SL moves the electron-energy state up, at the same time the electron miniband widens due to the increased extension of electron wave function into barrier layers. Thus, trying to increase the SL bandgap by only thinning the InAs layers can be problematic. To address these problems, a four-layer M-shape SL can be used,[12] where each SL period is composed of InAs/GaSb/AlSb/GaSb constituent layers. Cutoff wavelengths of $\sim 2.2\,\mu m$ at 300 K have been reported in InAs/GaSb/AlSb/GaSb M-shape SL detectors.[4] In this work, each period of the SL absorber is composed of InAs/GaSb/Al$_{0.8}$In$_{0.2}$Sb/GaSb layers, where compressive strained Al$_{0.8}$In$_{0.2}$Sb layers can provide flexibility to balance tensile strain of the InAs layers and to adjust the miniband width for carrier transport. Figure 1 contrasts the band structures for the simple two-layer and the four-layer M-shape SLs, in which the minibands and electron and hole wave functions for the ground states in the conduction and valence bands were calculated based on the two-band $k\cdot p$ model[13,14] for the two SLs. The $k\cdot p$ model has been used successfully by us and others for designing (or guiding the design of) interband cascade lasers and type-II SL based devices in the wavelength region from 2.7 to 11 μm over the last 20 years.[15–19] In this work, the $k\cdot p$ model was used

FIG. 1. Electron and hole wave functions and the related minibands for (a) four-layer M-shape SL and (b) two-layer SL. In both designs, the thicknesses of the layers were tailored to achieve similar cutoff wavelengths ($\sim 2.8\,\mu m$) at 300 K.

mainly for illustrating the difference between the simple two-layer and the four-layer M-shape SLs. Because of the absence of common atoms in the interfaces of InAs/GaSb SLs, there could be some uncertainties between experimentally determined bandgaps and the calculated values regardless of using the $k\cdot p$ model or any other theoretical model. For this reason, one needs to work closely with experiments to track possible variations every time. Moreover, the uncertainty and variations are more of a concern for laser devices with a narrow emission spectral linewidth compared to photodetectors with a broad response spectrum. To achieve a cutoff wavelength of $\sim 2.8\,\mu m$ in a two-component InAs/GaSb SL, the InAs thicknesses need to be 14 Å when the GaSb layer is chosen to be 30 Å thick (example shown Fig. 1(b)). A similar cutoff wavelength can be obtained by adding a thin Al$_{0.8}$In$_{0.2}$Sb layer to the SL structure in which the InAs layer can be as thick as 20 Å, while the GaSb layer thickness is kept at 30 Å. As shown in Fig. 1(a), the penetration of the wave functions into barrier layers decreases by inserting the Al$_{0.8}$In$_{0.2}$Sb layer in each SL period, resulting in narrower minibands in both conduction and valence band.

The two- and three-stage ICIPs presented in this paper were designed to target the SWIR band at room temperature. All the design parameters (electron and hole barriers, *etc*.) were the same for both ICIPs, only the number of stages were changed. To achieve a short cutoff wavelength ($<3\,\mu m$) at room temperature, we used an SL period composed of InAs/GaSb/Al$_{0.8}$In$_{0.2}$Sb/GaSb with thicknesses of 20, 15, 7, and 15 Å, respectively. The thin Al$_{0.8}$In$_{0.2}$Sb layer inserted in the middle of GaSb layers serves two main purposes. The larger lattice constant for Al$_{0.8}$In$_{0.2}$Sb layer (*cf.* the GaSb substrate) provides an extra degree of freedom to compensate the tensile strain induced by InAs layers. Also the insertion of this layer reduces the wave function penetration into barrier layers, resulting in narrower minibands than for a simple two-component InAs/GaSb SL. This makes the density of states (DOS) of the InAs/GaSb/AlSb/GaSb M-shape SL have more characteristics of two-dimensional (2D) DOS, which allows a sharper increase of the device absorption coefficient near its bandgap as compared to a 3D DOS.

Based on the reduction of quantum efficiency observed at high temperature in type-II superlattice detectors with absorber thicknesses in the range of 0.8–2 μm,[20,21] the high temperature diffusion length in superlattice structures is estimated to be on the order of 1 μm, which could vary with the material quality. Hence, we designed the thickness of individual absorbers in the ICIPs to be shorter than 1 μm. In the two-stage ICIP, the SL first (upper) and second absorbers were 570 and 644 nm thick, respectively, and in the three-stage ICIP, the additional third absorber was 741 nm thick, as indicated in Figs. 2(a) and 2(b). The absorbers in the optically deeper stages were made thicker to achieve photocurrent matching across the stages. Figure 2(c) shows the calculated band structure using the two-band $k\cdot p$ model. The ground states and their corresponding wave functions are plotted for quantum wells in the hole and electron barriers. Minibands in SL structure were calculated using a 2-band Kronig-Penny model. For clarity, only 10 SL periods of the
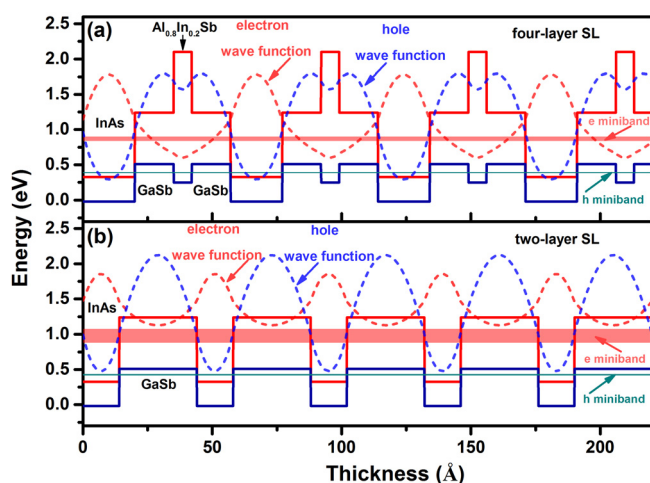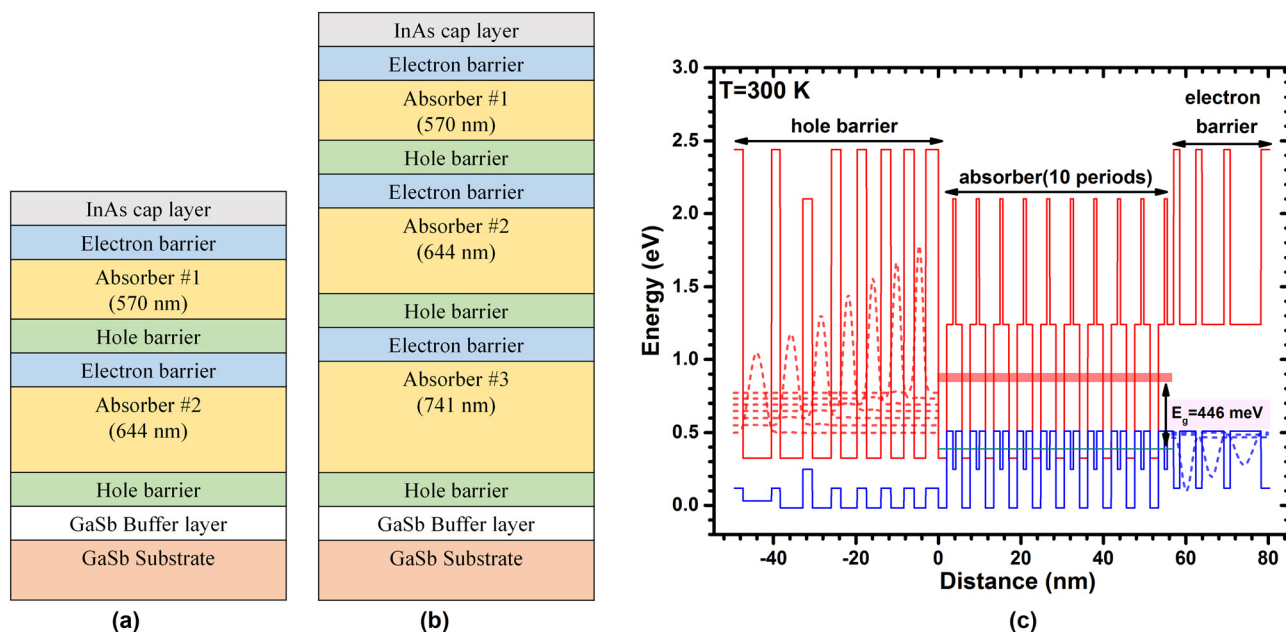
FIG. 2. Schematic structure for (a) two- and (b) three-stage ICIPs. (c) Band structure: showing ground states and their corresponding wave functions as calculated using a two-band *k·p* model. Electron barriers were made of three GaSb/AlSb quantum wells with 39, 53, and 75 Å thick GaSb wells. Hole barriers were composed of seven InAs/Al(In)Sb quantum wells with 25, 31.5, 35, 39.5, 46, 55, and 69 Å thick InAs wells.

absorber are shown, whereas the actual SL absorber consists of hundreds of periods.

B. Device growth and fabrication

The ICIP structures were grown by molecular beam epitaxy (MBE) on GaSb substrates. Figure 3 shows the high resolution X-ray diffraction (HRXRD) scans for the two detector structures. Both structures have compressive strain relative to the GaSb substrate. The lattice mismatch is 0.089% and 0.108% in the two- and three-stage ICIPs, respectively. The FWHM for the 0th order peaks are 20 and 28 arc sec in the two- and three-stage ICIPs, respectively (see inset, Fig. 3).
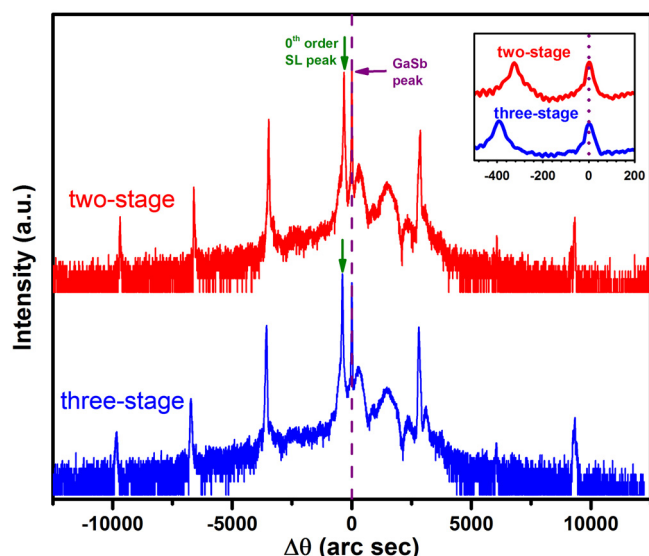

FIG. 3. HRXRD scans for two- and three-stage ICIPs. Both ICIPs had compressive strain relative to the GaSb substrate.

These scans indicate that the two- and three-stage ICIP structures are comparable in terms of material quality.

Using contact lithography and wet etching, the grown wafers were processed into a series of square mesa detectors with edge lengths varying from 50 to 1000 μm. Next a passivation layer consisting of 190 nm of Si_xN_y followed by 160 nm of SiO_2 was RF-sputter deposited. Finally, Ti/Au contacts were deposited and the detectors were wire bonded for characterization.

III. RESULTS AND DISCUSSION

A. Electrical characteristics

The current density (J)–voltage (V) characteristics of ICIPs were measured at 250 to 340 K (250 K can be achieved using one-stage thermoelectric coolers). For a representative 500×500 μm^2 detector from the two-stage (three-stage) wafer, dark current density at -50 mV was 4.7×10^{-4} A/cm^2 (2.6×10^{-4} A/cm^2) at 250 K. The dark current density increased to 1.0×10^{-2} A/cm^2 (0.67×10^{-2} A/cm^2) at 300 K, for the same bias. Figure 4 shows the dark current densities for three different sized ICIPs made from both two- and three-stage wafers. As can be seen in Fig. 4, dark current densities were larger in smaller size detectors for both two- and three-stage ICIPs throughout the temperature range. The size-dependent dark current densities were attributed to the imperfect passivation and related surface states. Another factor is the rough side walls associated with the wet etching process, caused by the different etch rates in different layers of the structure. Rough side wall surfaces make reliable and consistent passivation difficult. Such mesa-size dependence has also been reported for the mature $In_xGa_{1-x}As$ SWIR detectors and other III-V based short-wave IR photodetectors at room temperature.[22,23] While there has been some
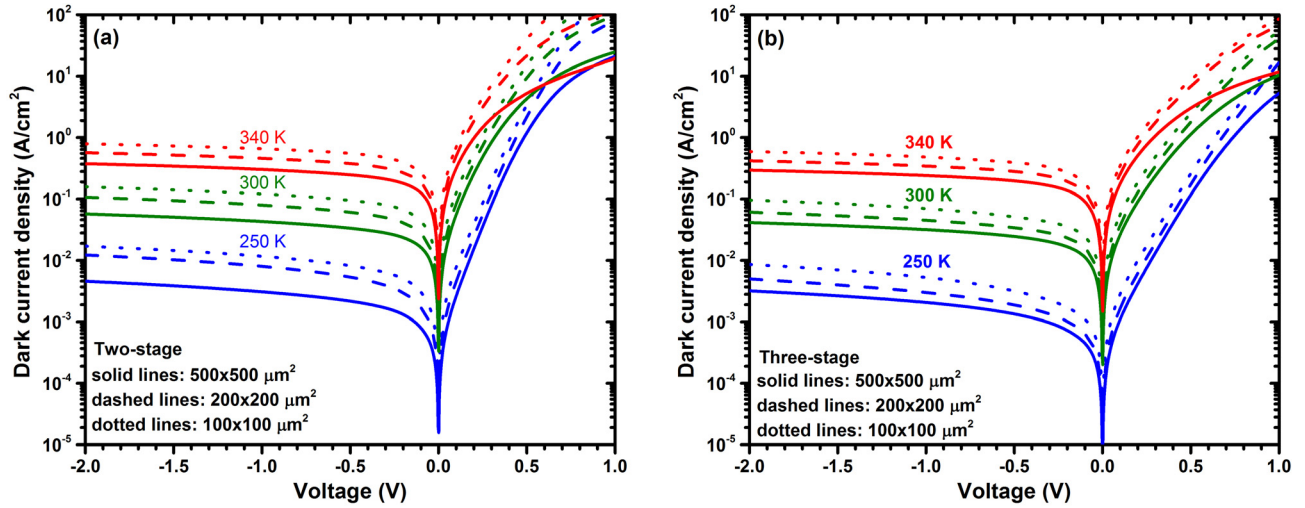
FIG. 4. Dark current densities for 250–340 K for (a) two- and (b) three-stage SWIR ICIPs. The densities were larger for smaller size detectors indicating the side walls and the device passivation need to be improved.

progress in this area, the surface leakage issue has not been fully resolved in these materials and has remained as one of the major unresolved issues for III-V based, specifically type-II SL, infrared detectors.[24]

To investigate the size dependent behavior of the dark current density, the product of zero-bias resistance and device area (R_0A) for the different sized ICIPs are plotted as a function of the perimeter (P) to area (A) ratio. The contribution of bulk and surface currents on the device R_0A can be separated by fitting the device R_0A to the equation[25]

$$\frac{1}{R_0A} = \left(\frac{1}{R_0A}\right)_{Bulk} + \frac{1}{\rho_{sw}}\left(\frac{P}{A}\right), \qquad (1)$$

where ρ_{sw} is the device sidewall resistivity. Figure 5(a) shows the size dependent R_0A for two- and three-stage ICIPs at 300 K. The extracted $(R_0A)_{Bulk}$ and sidewall resistivities (ρ_{sw}) were larger in three-stage ICIPs compared to the two-stage ICIPs in this temperature range. Table I summarizes these fitting parameters for the different operating temperatures.

An Arrhenius plot of device R_0A over the temperature range for the different sized ICIPs allows us to determine the activation energy of the dominant dark current mechanism that give rise to the observed temperature variation. This amounts to fitting the device R_0A to

$$\frac{1}{(R_0A)} \approx Ce^{-\frac{E_a}{k_BT}}, \qquad (2)$$

where E_a, T, k_B, and C are the activation energy, temperature (K), Boltzmann constant, and fitting prefactor, respectively. Figure 5(b) shows the Arrhenius plots for the different detector sizes. These Arrhenius plots show the expected linear behavior. Table II summarizes these activation energies.

The activation energies are slightly larger for the three-stage in comparison with those for the two-stage ICIPs, for all different sizes. Also, activation energies were lower in ICIPs with smaller sizes for the two- and three-stage devices. In order to specifically investigate the effect of surface leakage on the device activation energy, $(R_0A)_{Bulk}$ and sidewall
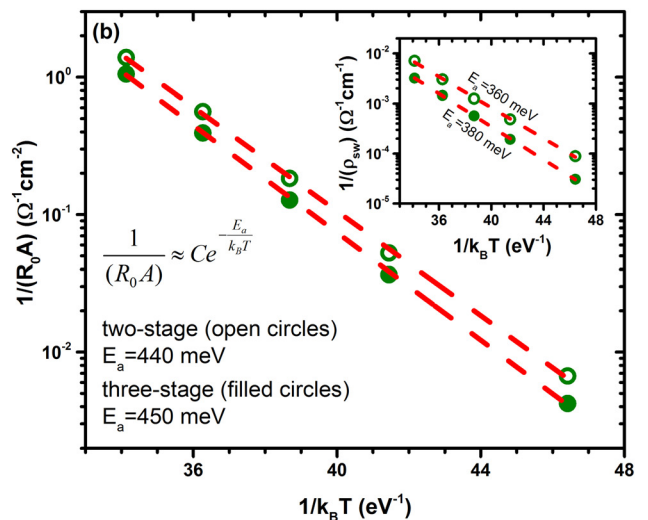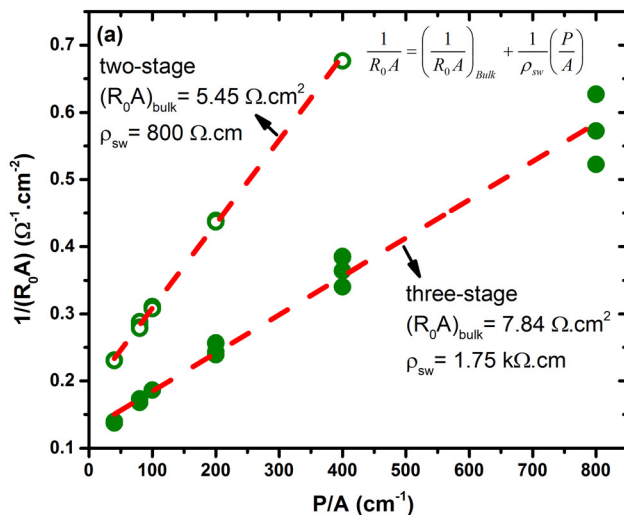

FIG. 5. (a) Size dependent R_0A for two- and three-stage SWIR ICIPs at 300 K. Side-wall resistivity and bulk R_0A were larger in three-stage detectors compared to the two-stage detectors. (b) Arrhenius plot of bulk and surface (inset) activation energies for two- and three-stage ICIPs.

TABLE I. Summary of the bulk and surface contributions to the device R_0A for 250–340 K in two- and three-stage ICIPs.

Temperature (K)	Two-stage		Three-stage		$\dfrac{R_0A_{3-stage}}{R_0A_{2-stage}}$
	$(R_0A)_{bulk}$ (Ω cm^2)	ρ_{sw} (kΩ cm)	$(R_0A)_{bulk}$ (Ω cm^2)	ρ_{sw} (kΩ cm)	
250	149	11.2	237	32.6	1.59
280	19.1	2.07	27.3	5.19	1.43
300	5.45	0.80	7.84	1.75	1.35
320	1.78	0.33	2.54	0.69	1.43
340	0.72	0.14	0.95	0.31	1.32

resistivities (ρ_{sw}) obtained from size dependent analysis of R_0A were fitted to Eq. (2). Bulk activation energies were close to the device bandgap. The extracted activation energies for the side wall resistivity were 360 meV (380 meV) in two-stage (three-stage) ICIPs. These numbers were larger than the half of the bandgap ($\sim$240 meV) and were about 75% and 80% of the bandgap energy in two- and three-stage ICIPs, respectively. Because surface states were more influential on small size ICIPs, the device activation energy had a larger reduction from the bulk activation energy and approached the side wall activation energy for small size ICIPs. This observed reduction in activation energy for smaller size ICIPs suggests a degree of side-wall leakage current through surface states. Activation energies close to the bulk limit can be achieved with improved sidewall passivation.

It is instructive to compare the experimental values of R_0A to the theoretical values for an ideal ICIP.[7] For an ideal device, diffusion current is the only mechanism that contributes to R_0A. Because diffusion current often dominates the device dark current at high temperatures, the measured R_0A is expected to agree better with predicted R_0A at high temperatures. In this "diffusion-limited" model, the ratio of R_0A between the three- and two-stage ICIPs with absorber lengths shorter than the minority-carrier diffusion length can be approximated as

$$\frac{R_0A_{3-stage}}{R_0A_{2-stage}} \approx \frac{d_1 d_2 + d_1 d_3 + d_2 d_3}{(d_1 + d_2) d_3}, \tag{3}$$

where d_1, d_2, and d_3 are the absorber thickness in corresponding stages. For the absorber thickness used in our structures the ratio is 1.41, which is in good agreement with the experimental value of 1.35, at 300 K, for the bulk R_0A. As discussed below, the device zero-bias photo-response did not decrease by increasing the device temperature for 250–340 K, which validates this approximation for these detectors. The effects of series and other parasitic resistances, which become more

influential at elevated temperatures, were not excluded from the measurement data. Such effects may explain the small deviations from theory observed at certain temperatures.

B. Optical characteristics

The optical response of the ICIPs was collected using an IR glow-bar source within an FTIR spectrometer and calibrated using an 800 K blackbody source (aperture diameter 1.52 cm). Figure 6(a) shows the calibrated responsivity for the two- and three-stage ICIPs for 250–340 K. The zero-bias response did not show an appreciable decrease for an increase in the device temperature for both two- and three-stage ICIPs. This behavior implies that the thickness of the individual absorber in each stage was shorter than the diffusion length and did not limit the carrier transport and collection up to 340 K. The zero-bias response at 2.1 μm and 300 K was 0.44 and 0.37 A/W for two- and three-stage ICIPs, respectively. While the two ICIPs were designed to be photo-current matched, photo-response was $\sim$16% lower in the three-stage ICIP at this wavelength. This suggests the possible imperfect photo-current matching between individual stages and perhaps larger photo-current mismatch in the three-stage ICIP. The current mismatch can be minimized by adjusting thicknesses of the absorbers so that the photo-response can be improved for both ICIPs.

The detectors photo-response was also measured under different reverse bias (see Fig. 6(b)). At $\lambda = 2.1$ μm and 300 K, the device maximum photo-response increased by 18% and 24% under reverse bias in two- and three-stage ICIPs, respectively. This small dependence of photo-response on bias voltage may be caused by the combination of imperfect metal contact to semiconductor surfaces (non-ideal Ohmic contacts) and some degree of misalignments of energy levels between quantum wells and adjacent stages. When the contacts and alignments of energy levels in every region are optimized, such a bias-voltage dependence of the photo-response can be eliminated and the maximum photo-response can be obtained under zero-bias condition. This

TABLE II. Activation energies for different detector sizes of the two- and three-stage detectors for 250–340 K. Bulk and sidewall activation energies refer to the Arrhenius fit for $(R_0A)_{Bulk}$ and ρ_{sw} extracted from the size dependent analysis of R_0A.

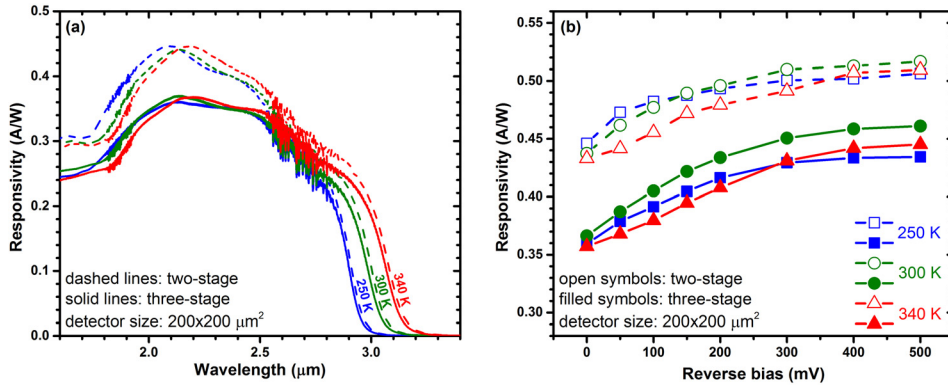| Detector	E_g (0 K) (meV)	Activation energy (meV)					
		200×200 μm^2	400×400 μm^2	500×500 μm^2	1000×1000 μm^2	Bulk	Side wall
Two-stage	480	390	410	410	420	440	360
Three-stage	480	430	420	430	450	450	380

FIG. 6. (a) Zero-bias responsivity for representative two- and three-stage ICIPs at 250–340 K. (b) Photo-response (at 2.1 μm) vs. reverse bias in two- and three-stage ICIPs for 250–340 K.

small bias-dependence of photoresponse and its correlation with either a possible Schottky barrier at the contact layer or band misalignments in different regions of the structure will be investigated and further clarified in our future work.

The performance of the ICIPs can further be examined by comparing their normalized detectivities (D^*). By considering Johnson and shot noise as the only noise sources and neglecting the surface current, the normalized detectivity can be calculated using[8]

$$D^* = \frac{R_\lambda}{\sqrt{\dfrac{4k_BT}{RA} + \dfrac{2qJ_d}{N_s}}}, \qquad (4)$$

where R_λ, RA, J_d, and N_s are the device responsivity, resistance area product, dark current density, and number of stages, respectively. For ideal ICIPs, larger RA and smaller J_d are expected in a three-stage device compared to a similar two-stage device. Also, the shot noise term ($\frac{2qJ_d}{N_s}$) in Eq. (4) is inversely proportional to the number of stages. If surface currents, which typically bypass the cascade stages, are taken into consideration, Eq. (4) should be modified to

$$D^*_{Mod} = \frac{R_\lambda}{\sqrt{\dfrac{4k_BT}{RA} + \dfrac{2qJ_d}{N_s} + 2qJ_s}}, \qquad (5)$$

where J_d is the part of the total dark current density that passes through the multiple stages, and J_s is the surface current density that leaks through side walls without going across multiple interband transitions. From Eq. (5), one can see that even for the same level of dark current (for the case of negligible surface currents), a three-stage ICIP will have

lower shot noise in comparison with a two-stage ICIP. Indeed, lower shot noise (*cf.* conventional single stage detectors) has been observed in MWIR ICIPs by direct noise measurements.[26]

Because of the size dependent dark current density, the device D^* was also size dependent. For instance, at 250 K D^* was 4.1×10^{10} and 3.1×10^{10} cm Hz$^{1/2}$/W for representative $1000 \times 1000\ \mu m^2$ and $200 \times 200\ \mu m^2$ three-stage ICIPs, respectively. Figure 7 shows the normalized detectivity under zero-bias for two- and three-stage ICIPs ($200 \times 200\ \mu m^2$) at different temperatures. Calculated Johnson-noise-limited D^* (for $\lambda = 2.1\ \mu m$) was 3.1×10^{10} (2.5×10^{10}) and 5.8×10^9 (5.1×10^9) cm Hz$^{1/2}$/W for the three-stage (two-stage) ICIP at 250 and 300 K, respectively. If diffusion current controls the device dark current, the device resistance will exponentially increase with reverse bias within a certain range. This means even if the device signal does not increase with reverse bias, D^* could increase under reverse bias condition. The maximum calculated D^* at 300 K was 7.5×10^9 (5.6×10^9) cm Hz$^{1/2}$/W for the three-stage (two-stage) ICIP and was obtained under -300 mV (-100 mV) reverse bias. However, other sources of noise, such as $1/f$ noise, usually increase rapidly under reverse bias and often negate the benefits of the larger device resistance obtained under a reverse bias condition.[27] This D^* is close to 2.8×10^{10} cm Hz$^{1/2}$/W, the value claimed by Judson Technologies for a commercial 2.8 μm cutoff $Hg_{1-x}Cd_xTe$ detector at 295 K.[28] The device normalized detectivity was larger in the three-stage ICIP at all temperatures, demonstrating the benefits of the three-stage detector over the two-stage detector. Because D^* is directly proportional to the device responsivity, D^* in the three-stage ICIP can be increased by improving the photo-current matching. Considering that the
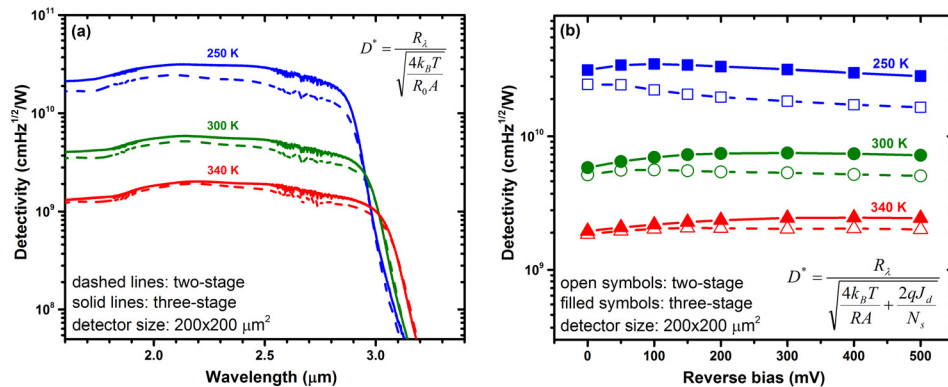

FIG. 7. (a) Normalized detectivity (FOV = 2π sr) for two- and three-stage ICIPs under zero-bias condition for 250–340 K. (b) Normalized detectivity vs. reverse bias for the same ICIPs. Detectors were covered with a copper shield (at the device temperature) during dark current measurements.

total thickness (1.96 μm) of absorbers in the three-stage ICIP structure is less than 2 μm, ICIPs with more stages should further increase absorption efficiency and suppress noise, resulting in improved device performance. More stages will present challenges including device design for better current matching, material quality for longer growth times, and device fabrication/passivation for more interfaces. However, such advancement is possible with improved understanding and knowledge of the material properties, MBE growth technology, as well as device fabrication techniques.

IV. SUMMARY AND CONCLUSIONS

Two- and three-stage SWIR ICIPs were successfully demonstrated at high temperatures. The photo-response of these ICIPs showed no decrease at high temperatures. This implies that ICIPs can circumvent the diffusion length limitation on carrier transport at high temperatures (at least up to 340 K). Values of Johnson-noise-limited detectivity D^* exceeding 10^9 cm Hz$^{1/2}$/W were obtained at temperatures up to 340 K. The value of D^* was larger in the three-stage ICIP for all measured temperatures compared to the two-stage ICIP, confirming the benefits of ICIPs with more stages. Size dependent analysis of the R_0A for devices indicates that the surface current was significant in small size ICIPs, which contributed to the dependence of the activation energies for these ICIPs. Better device performance is expected by improving the device fabrication/passivation and optimizing the device structure for better photo-current matching in ICIPs with more stages.

ACKNOWLEDGMENTS

[1]D. L. Smith and C. Mailhiot, J. Appl. Phys. **62**, 2545 (1987).

[2]C. H. Grein, P. M. Young, and H. Ehrenreich, Appl. Phys. Lett. **61**, 2905 (1992).

[3]B. Tang, Y. Q. Xu, Z. Q. Zhou, R. T. Hao, G. W. Wang, Z. W. Ren, and Z. C. Niu, Chin. Phys. Lett. **26**, 028102 (2009).

[4]A. M. Hoang, G. Chen, A. Haddadi, S. A. Pour, and M. Razeghi, Appl. Phys. Lett. **100**, 211101 (2012).

[5]A. Haddadi, X. V. Suo, S. Adhikary, P. Dianat, R. Chevallier, A. M. Hoang, and M. Razeghi, Appl. Phys. Lett. **107**, 141104 (2015).

[6]J. Piotrowski and W. Gawron, Infrared Phys. Technol. **38**, 63 (1997).

[7]R. T. Hinkey and R. Q. Yang, J. Appl. Phys. **114**, 104506 (2013).

[8]R. Q. Yang, Z. Tian, Z. Cai, J. F. Klem, M. B. Johnson, and H. C. Liu, J. Appl. Phys. **107**, 054514 (2010).

[9]J. V. Li, R. Q. Yang, C. J. Hill, and S. L. Chuang, Appl. Phys. Lett. **86**, 101102 (2005).

[10]H. Lotfi, L. Li, H. Ye, R. T. Hinkey, L. Lei, R. Q. Yang, J. C. Keay, T. D. Mishima, M. B. Santos, and M. B. Johnson, Infrared Phys. Technol. **70**, 162 (2015).

[11]H. Lotfi, L. Lei, L. Li, R. Q. Yang, J. C. Keay, M. B. Johnson, Y. Qiu, D. Lubyshev, J. M. Fastenau, and A. W. K. Liu, Opt. Eng. **54**, 063103 (2015).

[12]B.-M. Nguyen, D. Hoffman, P.-Y. Delaunay, and M. Razeghi, Appl. Phys. Lett. **91**, 163511 (2007).

[13]E. O. Kane, J. Phys. Chem. Solids **12**, 181 (1960).

[14]R. Q. Yang and J. M. Xu, Phys. Rev. B **46**, 6969 (1992).

[15]R. Q. Yang, Microelectron. J. **30**, 1043 (1999).

[16]R. Q. Yang, in *Semiconductor Lasers: Fundamentals and Applications*, edited by A. Baranov and E. Tournie (Woodhead Publishing Limited, Cambridge, UK, 2013), pp. 487–513.

[17]I. Vurgaftman, R. Weih, M. Kamp, J. R. Meyer, C. L. Canedy, C. S. Kim, M. Kim, W. W. Bewley, C. D. Merritt, J. Abell, and S. Höfling, J. Phys. D: Appl. Phys. **48**, 123001 (2015); and references therein.

[18]S. B. Rejeb, M. Debbichi, M. Said, A. Gassenq, E. Tournie, and P. Christol, J. Appl. Phys. **108**, 093107 (2010).

[19]Y. Livneh, P. C. Klipstein, O. Klin, N. Snapi, S. Grossman, A. Glozman, and E. Weiss, Phys. Rev. B **86**, 235311 (2012).

[20]Y. Wei, A. D. Hood, H. Yau, A. Gin, M. Razeghi, M. Z. Tidrow, and V. Nathan, Appl. Phys. Lett. **86**, 233106 (2005).

[21]J. V. Li, C. J. Hill, J. M. Mumolo, S. D. Gunapala, S. Mou, and S.-L. Chuang, Appl. Phys. Lett. **93**, 163505 (2008).

[22]F. Rutz, P. Kleinow, M. Walther, R. Aidam, W. Bronner, L. Kirste, J. Niemasz, R. Rehm, J. Schmitz, T. Stadelmann, M. Wauro, A. Wörl, A. Sieck, and J. Ziegler, Proc. SPIE **8993**, 89930W (2013).

[23]J. P. Prineas, J. Yager, S. Seyedmohamadi, and J. T. Olesberg, J. Appl. Phys. **103**, 104511 (2008).

[24]M. Kinch, *State-of-the-Art Infrared Detector Technology* (SPIE Press, Bellingham, USA, 2014).

[25]H. K. Chung, M. A. Rosenberg, and P. H. Zimmermann, J. Vac. Sci. Technol. A **3**, 189 (1985).

[26]L. A. Treider, V. M. Cowan, C. P. Morath, Z. Tian, and S. Krishna, Proc. SPIE **8876**, 88760B (2013).

[27]M. B. Reine, in *Infrared Detectors and Emitters: Materials and Devices*, edited by P. Capper and C. T. Elliot (Kluwer Academic Publishers, 2000), pp. 311–376.

[28]*Photovoltaic Mercury Cadmium Telluride Detectors* (Teledyne Judson Technologies, Montgomeryville, PA 18936, 2003).